A&A, 707, A53 (2026)
https://doi.org/10.1051/0004-6361/202557541
© The Authors 2026

Astronomy & Astrophysics

Understanding the chemistry of temperate exoplanet atmospheres through experimental and numerical simulations

O. Sohier[1,*], A. Y. Jaziri[1], L. Vettier[1], A. Chatain[1], T. Drant[2], and N. Carrasco[1,3]

[1] LATMOS/IPSL, UVSQ Université Paris-Saclay, Sorbonne Université, CNRS, Guyancourt, France
[2] ETH University, Center for Origin and Prevalence of Life, Department of Earth and Planetary Sciences, 8092 Zurich, Switzerland
[3] ENS-Paris-Saclay, Gif sur Yvette, France

Received 3 October 2025 / Accepted 17 December 2025

ABSTRACT

Context. Characterizing temperate exoplanet atmospheres remains challenging due to their small size and low temperatures. Recent JWST observations provide valuable data, but their interpretation has led to diverging conclusions, highlighting the limitations of observations alone. Complementary approaches combining laboratory experiments and photochemical modeling are essential for constraining atmospheric chemistry and interpreting observations.

Aims. This study investigates out-of-equilibrium chemistry in the upper atmospheres of H_2-dominated temperate sub-Neptunes enriched in carbon-bearing species (CH_4, CO, or CO_2). We aim to identify chemical pathways governing the formation and evolution of neutral species and to assess their sensitivity to key parameters such as C/O ratio and metallicity.

Methods. Our approach combines experimental and numerical simulations on H_2-rich gas mixtures representative of sub-Neptune atmospheres and spanning a wide range of CH_4, CO, and CO_2 mixing ratios. We used a cold plasma reactor to simulate out-of-equilibrium upper-atmospheric chemistry. Chemical evolution was tracked by mass spectrometry and infrared spectroscopy (IR). A 0D photochemical model was used to reproduce reactor conditions, guiding interpretation of the key pathways and abundance trends.

Results. We observed the formation of both reduced and oxidized organic compounds. In CH_4-rich mixtures, hydrocarbons formed efficiently through methane chemistry, correlating with CH_4 concentration and agreeing with models. In more oxidizing environments, particularly CO_2-rich mixtures, hydrocarbon formation was inhibited by complex reaction networks and oxidative losses. We find that oxygen incorporation enhances chemical diversity and promotes the formation of oxidized organic compounds of prebiotic interest (H_2CO, CH_3OH, CH_3CHO), especially in atmospheres containing both CH_4 and CO_2. Atmospheres containing CH_4 and CO – which balance carbon and oxygen supply without excessive oxidative destruction – favor efficient production of hydrocarbons and oxidized compounds.

Conclusions. Out-of-equilibrium chemistry plays a key role in the diversification and organic complexification of temperate exoplanet atmospheres. Combining laboratory experiments with photochemical modeling elucidates pathways to hydrocarbon and oxidized organic formation. Studying detectability of these photoproducts with JWST and new high-resolution ground-based instruments is an important focus for future studies.

Key words. methods: laboratory: molecular – methods: numerical – planets and satellites: atmospheres

1. Introduction

Characterizing the atmospheres of temperate exoplanets presents significant challenges due to their small size and relatively cold temperatures, making them difficult to detect and study. These exoplanets, which have an equilibrium temperature below ~500 K, can be classified into three categories: terrestrial planets, super-Earths, and sub-Neptunes. To date, no terrestrial exoplanets, including those in the TRAPPIST-1 system, have been clearly and robustly detected as having an atmosphere (Gillon et al. (2025) for TRAPPIST-1b and c, Piaulet-Ghorayeb et al. (2025) for TRAPPIST-1d, Espinoza et al. (2025); Glidden et al. (2025) for TRAPPIST-1e). On the other hand, sub-Neptunes and super-Earths – which to this day are the most commonly detected types and therefore dominate the population of known exoplanets (Fressin et al. 2013; Luger & Barnes 2015; Owen & Mohanty 2016; Van Eylen et al. 2018; Hardegree-Ullman et al. 2019) – have emerged as ideal targets for atmospheric characterization. In particular, those orbiting M dwarf stars have a unique advantage known as the "M dwarf opportunity," because the smaller size and lower brightness of the host star improve the signal-to-noise ratio during observations. This results in larger transit depths, making it easier to detect and study planetary atmospheres (Cabot et al. 2024; Doyon 2024). These planets are also particularly intriguing because they have no direct analogs in our Solar System. This raises fundamental questions about the processes that shape their atmospheres, interiors, formation, and habitability (Cabot et al. 2024). In addition, a significant number of planets orbiting M dwarfs reside in their star's temperate zone (Dressing & Charbonneau 2015), making the question of their habitability all the more interesting. This habitability is challenged by the unique environmental conditions around M dwarfs, including intense stellar flares, high-energy particle events, and limited ultraviolet flux to drive prebiotic chemistry (Scalo et al. 2007; Ricker et al. 2015; Shields et al. 2016; Rimmer et al. 2018).

Recent advancements in observational techniques, particularly with instruments on the James Webb Space Telescope

* Corresponding author: orianne.sohier@latmos.ipsl.fr

Open Access article, published by EDP Sciences, under the terms of the Creative Commons Attribution License (https://creativecommons.org/licenses/by/4.0), which permits unrestricted use, distribution, and reproduction in any medium, provided the original work is properly cited.
This article is published in open access under the Subscribe to Open model. Subscribe to A&A to support open access publication.

(JWST), have made these planets favorable targets. In particular colder exoplanets, with temperatures between 500 and 1000 K, tend to have clearer atmospheres, as they are less obscured by clouds and hazes (Morley et al. 2015; Brande et al. 2024; Yang & Hu 2024; Gao et al. 2021). The advancements have already led to the successful characterization of two temperate sub-Neptune exoplanetary atmospheres, marking significant progress in this field. The analysis of transit spectroscopy data from the atmospheres of K2-18 b (Madhusudhan et al. 2023) and TOI-270 d (Benneke et al. 2024; Holmberg & Madhusudhan 2024) has highlighted atmospheric compositions dominated by hydrogen and containing a few percent of carbon-bearing species, such as methane or carbon dioxide. Despite these revolutionary new data, their atmospheric composition is still poorly constrained and highly debated.

In the case of K2-18 b, initial JWST observations in the 0.9–5.2 µm range combined with data from NIRISS SOSS and NIRSpec G235H instruments acquired in 2023 suggest the presence of CH_4 and CO_2 at comparable levels, around 1% each (Madhusudhan et al. 2023). Subsequent studies incorporating non-equilibrium chemistry have led to a revised interpretation, indicating a higher level of CH_4 and a lower abundance of CO_2 (Wogan et al. 2024). This reinterpretation is supported by a new analysis of the JWST data, which has called into question the initial detection of CO_2 as a whole (Schmidt et al. 2025). In 2024 and early 2025, four new transit observations were acquired with the NIRSpec G395H instrument and presented by Hu et al. (2025). By stacking all NIRSpec spectral data obtained to date, they report a significant detection of both CH_4 and CO_2, with upper limits of approximately 10% and 1% respectively, supporting the hypothesis of a predominance of methane. Meanwhile, initial data were also acquired with the JWST MIRI LRS instrument in the 6–12 µm range, and primary analysis of the data did not provide strong evidence for CH_4 or CO_2 (Madhusudhan et al. 2025), which do not show clear bands in this range.

The detection of signatures of minor atmospheric constituents also remains largely unconstrained by these low-resolution observations. Non-equilibrium chemistry models help characterize the complete atmospheric composition, but they require observational constraints such as metallicities and C/O ratios, which are also poorly known. They predict the abundance of various components, even minor ones for which signatures remain undetectable in observations. According to these simulations, CH_4, CO_2, CO, N_2, NH_3, H_2O, C_2H_4, and C_2H_6 could be major species, up to the percent range (Jaziri et al. 2025; Luque et al. 2025). Jaziri et al. (2025) also predict that oxidized species such as H_2CO, CH_3OH, and CH_3CHO can reach mixing ratios close to the parts-per-million level. These molecules are of significant prebiotic interest. H_2CO is important as a possible precursor to sugars through the formose reaction, which is key for the origin of the RNA or pre-RNA world (Butlerow 1861; Cleaves 2008). CH_3OH is a key synthon in the RNA world (Mathew et al. 2022). Aldehydes, such as H_2CO and CH_3CHO, are key precursors of several amino acids through the Strecker synthesis (Strecker 1850). The atmospheric photochemical production of these oxidized compounds has already been identified as one of the main sources of these compounds in the atmosphere of primitive Earth (Pinto et al. 1980; Wen et al. 1989). It is therefore worthwhile to study their formation pathways in temperate exoplanetary atmospheres.

If we are to overcome the major scientific challenge of characterizing the chemistry of temperate exoplanet atmospheres, a synergy between the observational, modeling, and experimental communities is required. Initiatives of this type are already underway in the community. One example is the attempt to obtain experimental data on the temperature-dependent photoabsorption cross sections of key molecules such as CO_2, which provide essential data for atmospheric models of hot exoplanets (Venot et al. 2013, 2018). For the cooler exoplanets, studies have been carried out on the detectability of ions in the thermosphere of sub-Neptunes by combining laboratory experiments, chemical modeling, and simulated observations as well as in the atmospheres of super-Earths by combining laboratory measurements and a 0D photochemical model (Bourgalais et al. 2020, 2021).

A few experiments have been developed for the characterization of the atmospheres of exoplanets, and they mainly focus on the formation and properties of haze and aerosols in the atmospheres of super-Earths and sub-Neptunes (Gavilan et al. 2018; He et al. 2018a,b; Hörst et al. 2018; Moran et al. 2020; Jiménez-Escobar et al. 2025) or hot Jupiters (Fleury et al. 2019, 2020, 2023). Studies focusing on the neutral gas phase chemistry in the atmospheres of cool exoplanets are quite rare. He et al. (2019) conducted laboratory experiments on a wide range of exoplanet atmospheres, with a wide variety of metallicities (100×, 1000×, and 10 000× solar metallicity) and temperatures (at 300, 400, and 600 K) and for warmer H_2-rich atmospheres (800 K, 100×, and 1000× solar metallicities (He et al. 2020)). They explored the effect of different types of irradiation, using a cold plasma or a UV photon lamp as energy sources. They found that a complex non-equilibrium chemistry occurred, leading to the formation of potential haze-forming precursors. Wang et al. (2025) explored CO_2-rich atmospheres at 300 and 500 K, with a 2000x solar metallicity. Under plasma irradiation, they observed the formation of various hydrocarbons and oxygen- and nitrogen-containing species, and they identified reactive gas precursors for haze formation such as C_2H_4, H_2CO, and HCN. However, the analytical diagnosis of all these studies was based solely on residual gas analyzer mass spectrometry (RGA MS), which led to an uncertain identification of some compounds. Reed et al. (2024) studied the UV irradiation of $H_2S/CH_4/N_2$ gas mixtures, with or without CO_2, at an ambient temperature (around 300 K). They analyzed the gas-phase products using gas chromatography equipped with sulfur chemiluminescence detection (GC-SCD), a diagnostic tool less ambiguous than RGA MS. They were thus able to demonstrate the abiotic production of several organosulfur gases, limiting their robustness as biosignatures.

The aim of this work is to propose chemical mechanisms occurring in a wide range of possible atmospheric compositions of temperate sub-Neptunes. In this context, we carried out parallel experimental and 0D numerical simulations to understand the complex out-of-equilibrium chemistry occurring in the upper layers of the H_2-dominated atmospheres of temperate exoplanets. These low-pressure atmospheric layers correspond to those probed by JWST observations and were exposed to energetic radiation that triggers photochemical processes. As the atmospheric composition of these exoplanets is unconstrained, we carried out a study on various $H_2/CH_4/CO/CO_2$ gas mixtures. The C/O ratio (from 0.5 to infinity) and metallicity (from 5 to 50 times the solar metallicity) of these mixtures are variable. The C/O ratio measures the relative abundance of carbon compared to oxygen, while metallicity measures the abundance of elements heavier than hydrogen and helium. To vary these parameters in our H_2-dominated gas mixtures, we used CH_4, CO, or CO_2 as the main component as well as different combinations of these carbon compounds. We chose to focus on these reactants because they allow us to obtain a wide range of

Table 1. Experimental compositions in percentages.

	Reduced mixtures				*Oxidized mixtures*								*$CH_4/CO/CO_2$ mixtures*											
H_2	99	97	95	90	99	97	95	90	99	97	95	90	98	94.5	94	94	90	98	94.5	94	94	90	97.5	89.5
CH_4	1	3	5	10									1	5	1	5	5	1	5	1	5	5	1	5
CO					1	3	5	10					1	0.5	5	1	5						1	5
CO_2									1	3	5	10						1	0.5	5	1	5	0.5	0.5
C/O ratio	∞	∞	∞	∞	1	1	1	1	0.5	0.5	0.5	0.5	2	11	1.2	6	2	1	5.5	0.6	3	1	1.25	1.75
Metallicity (compared to solar)	5.6	14.8	22.1	35.1	9.2	22.6	31.7	45.4	13.6	30.2	40.0	53.0	13.7	24.8	33.8	27.2	41.0	17.5	26.2	41.5	29.7	46.6	18.9	42.9

possible atmospheres based on the observational data currently available for K2-18 b. Of course, the reactants are relatively simplistic atmospheric analogs that do not take into account other elements such as nitrogen or sulfur, which may also be present in this type of atmosphere. Other oxygen-bearing molecules, such as water, could also be present in significant quantities in this atmosphere, although the upper layers may instead be dried out by cold trap processes (Charnay et al. 2021). Nevertheless, these atmospheric analogs already allow us to cover a wide range of atmospheric possibilities and to identify a great molecular diversity. A key aspect of this work lies in the combination of experiments and numerical simulations, which enables us to extract abundance trends and chemical formation pathways. Identifying key mechanisms enables us to understand the role of different carbon-bearing reactants (CH_4, CO, CO_2) in organic growth processes (i.e., carbon chains elongation) and to study the effect of oxygen incorporation on chemical diversification.

2. Methods

We studied the chemical evolution of atmospheric analog mixtures when irradiated in a cold plasma setup, mimicking photochemistry in the upper atmosphere. Complementary diagnoses were performed using mass spectrometry (MS) and infrared (IR) spectroscopy. In parallel, a 0D photochemical model predicted abundance values and reaction pathways, which we systematically compared with experimental results.

2.1. Mixtures of atmospheric analogs

Different gas mixtures were chosen to study a wide range of potential atmospheres, based on information gathered from observations of K2-18 b. These mixtures are dominated by hydrogen, with carbon-bearing compounds ranging from highly reduced carbon (CH_4) to an intermediate state (CO) to fully oxidized carbon (CO_2). To enable comparisons with planetary atmospheric models, the C/O ratios and metallicities of our mixtures are provided for reference. It should be noted that our compositions are set by the continuous gas flows in an open system. The gas residence time, i.e., the time spent by the gas in the irradiated medium, is set by the pressure and gas flow in our experiments and thus differ from the residence time found in atmospheric models. Thus, the C/O ratios given are enriched in CH_4, CO and CO_2, compared to atmospheric models. All mixtures are summarized in Table 1.

The most reduced atmospheres are composed of H_2 and CH_4. The relative proportions of H_2 and CH_4 vary in the experiments (see Table 1 for the relative mixing ratios). We refer to these mixtures as reduced mixtures. This type of atmosphere helps us characterize organic growth in the most reducing environment.

The more oxidized atmospheres are composed of H_2 and CO or CO_2. The relative mixing ratios are shown in Table 1. We refer to these mixtures as oxidized mixtures. This type of atmosphere allows us to explore the balance between adding carbon and oxygen atoms to the system.

The composite atmospheres combine the conditions of the reduced and oxidized atmospheres described above. They are composed of H_2, CH_4, CO and/or CO_2. A wide range of oxidation states is studied, as shown in Table 1.

2.2. Atmospheric simulation chamber

Experimental simulations of the upper atmospheric layers of temperate exoplanets were carried out using an experimental cold plasma device, the PAMPRE reactor (for Production d'Aérosols en Microgravité par Plasma REactif (Szopa et al. 2006)). This setup was initially developed to simulate the atmospheric chemistry of Titan, and the production of aerosol analogs (*tholins*) created by photochemistry in this atmosphere (Szopa et al. 2006; Quirico et al. 2008; Sciamma-O'Brien et al. 2010; Carrasco et al. 2012; Mahjoub et al. 2012; Fleury et al. 2014; Dubois et al. 2019, 2020). The use of this experimental platform has been extended over the years to include other atmospheres, such as early Earth (Fleury 2015; Fleury et al. 2017) or Pluto (Jovanovic 2021). More generally, the versatility of the experimental setup means we can study any temperate atmospheric chemical composition, which make it suitable for studying exoplanets. Initial research has already been carried out on organic aerosols produced in the atmospheres of Earth-like exoplanets (Gavilan et al. 2017, 2018).

PAMPRE induces a cold capacitively coupled radiofrequency plasma in a gaseous mixture, outside of thermodynamic equilibrium. This reproduces the energetic processes occurring in the upper layers of a temperate atmosphere exposed to energetic stellar particles and UV irradiation. It has been previously shown that the energy distribution of electrons in a nitrogen-dominated plasma reproduces the energy distribution of solar photons fairly accurately, with a slightly higher contribution in the VUV (Szopa et al. 2006). The stellar spectra of M dwarfs-around which the temperate exoplanets that interest us orbit-have higher UV radiation contributions than the Sun (France et al. 2013). This experimental setup is therefore appropriate for simulating the energetic environment of these exoplanetary atmospheres. Although our plasma is dominated by hydrogen, which may slightly alter the energy distribution of electrons, it remains adequate. These energetic processes trigger an imbalance in chemistry, dissociating gas molecules and allowing fragments to reorganize into new species. In specific cases, products even aggregate into solid particles, the tholins.

The setup consists of a cylindrical stainless steel reactor, 40 cm high and 30 cm in diameter, connected to a quadrupole mass spectrometer (QMS). High-pressure gas cylinders are connected to the setup via an injection manifold, enabling gas mixtures to be introduced into the main chamber. MKS mass flow meters, rated at 5, 10 and 100 standard cubic centimeters

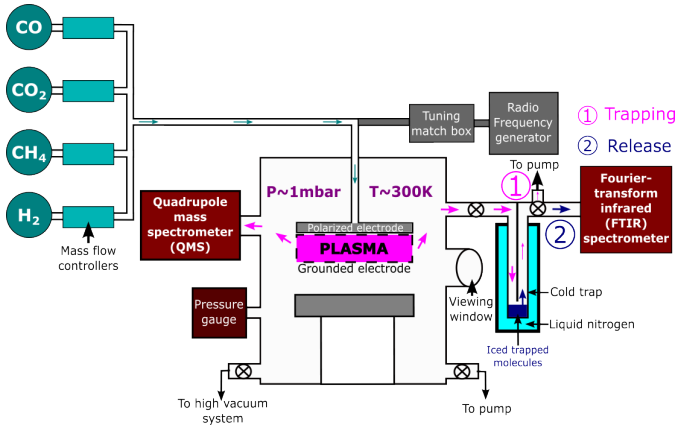

Fig. 1. Scheme of the plasma reactor PAMPRE.

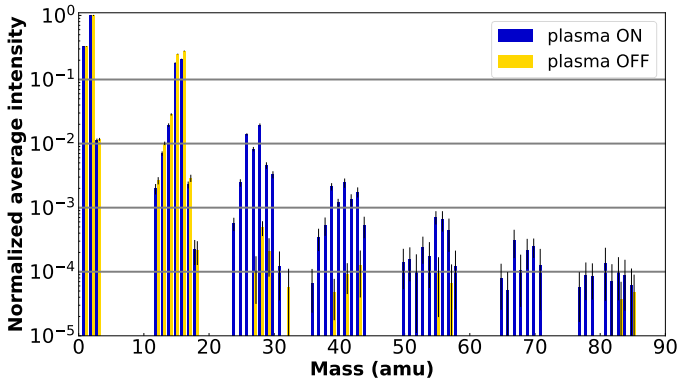

Fig. 2. Mass spectrum of a gas mixture of 95% H_2 plus 5% CH_4 before (gold) and during irradiation (blue).

per minute (sccm) with a full-scale accuracy of 1%, control the injection rates. The plasma is confined in a stainless steel cage measuring 13.8 cm in diameter and 5 cm in height, pierced with small holes to allow the gas to pass through. The top of this cage is the cathode, measuring 12.6 cm in diameter, polarized and powered by a 13.56 MHz generator. The gas mixture is injected into the reactor from the top of the chamber through the cathode, which is equipped with three superimposed grids to ensure a continuous, homogeneous injection flow. Gas flow rate is set at 40 sccm. The central grid, with a mesh size in the order of the Debye length (~0.1 mm), prevents the plasma from flowing back into the gas injection system. The gas mixture is extracted from the bottom of the chamber by a primary vane pump (Adixen by Pfeiffer Vacuum Pascal 2015 SD). This enables an open continuous-flow system, at 0.98 mbar and at ambient temperature (~300 K). A window allows visual monitoring of the plasma. Plasma discharge is only used in continuous mode in these experiments, with a power of 30 W. Between each experiment, the reactor is pumped with a turbomolecular pump (Adixen ATP 80) to achieve a secondary vacuum of around 1.5×10^{-6} mbar. A schematic diagram of the experimental setup is shown in Figure 1.

2.3. Mass spectrometry

Mass spectrometry is used as an analytical method to determine the molecular species produced. PAMPRE is equipped with a Hiden EQP system, which is used in residual gas analysis (RGA) mode, since only neutral species are considered in this study. A collector head is used to sample gaseous species through a 100 µm diameter orifice. The pressure inside the mass spectrometer is kept below $5\text{x}10^{-6}$ mbar. To study neutral species, an internal ionizer is used, with electron energy set at 70 eV. The resulting ions are then filtered and focused before entering the triple-filter mass analyzer, which detects masses from 1 to 200 m/z (mass-to-charge ratio) with a resolution of 1 atomic mass unit (amu). Finally, the ions arrive at an ion-counting detector – a secondary electron multiplier.

Several molecular fragments at different m/z values are generated and form a "fingerprint" specific to each molecule and incident electron energy, known as the fragmentation pattern. A full mass spectrum thus corresponds to the superposition of the fragmentation patterns of all the species present in the analyzed gas mixture. Reference fragmentation patterns were measured directly in the lab for the reactive compounds, i.e., H_2, CH_4, CO and CO_2. The reference fragmentation patterns of the products are extracted from the NIST Chemistry WebBook[1] (Linstrom & Mallard 2001).

All m/z over a selected mass range are scanned in BAR mode (Batched Analysis of Repetitions). This produces a histogram of peak intensities. Each mass spectrum contains 20 accumulated scans, over a mass range from 1 to 100 amu. A mass spectrum is taken at the initial state (spectrum OFF), when the gaseous mixture is injected inside the reactive chamber at 0.98 mbar, while the plasma discharge is still switched off. The plasma is switched on and after five minutes, a spectrum is taken (spectrum ON). To ensure that we had reached a stable steady state, we performed multiple ion detection when we activated the plasma. This allowed us to track several m/z ratios over time, thereby monitoring consumption and production and determining when we reach a stable state. In all our experiments, we observed stabilization after a maximum of 200 seconds.

The evolution of the gas composition can be seen by our plotting of the superposition of the two ON and OFF spectra (Figure 2). Our plotting of the difference of intensity between these two spectra (ON-OFF) reveals the production and destruction of the chemical species.

The measured mass spectra are processed first by removing the noise from the data: all intensities below 10 counts/s are removed, as the instrument's sensitivity is 10^6 counts/s maximum. Each spectrum is then normalized by its maximum intensity. In the direct-flow experiments, the maximum intensity is always at m/z 2 amu, corresponding to H_2. In trap-and-release experiments, the maximum intensity depends on the composition. Mean values and standard deviation at 95% are calculated from the 20 cycles for each m/z. If the difference between the average intensity and the standard deviation is below 10^{-6}, it is considered as noise and removed from the data.

While the reconstruction of a mass spectrum with fragmentation patterns works well with a few compounds, it becomes much more difficult to analyze and identify species in more complex mixtures with dozens of products. This is due to the superposition of several fragmentation patterns and the variability associated with these patterns – which depends on the geometry of the ion source, the mass-dependent filtering, and detection efficiency of the instrument. We therefore need a complementary analytical method in order to make unambiguous identifications.

[1] https://webbook.nist.gov/chemistry/

2.4. Infrared spectroscopy

Infrared spectroscopy was used to help identify species in $CH_4/CO/CO_2$ mixtures. The PAMPRE setup was connected to a multipass infrared white cell with an optical beam length of 10 m. The cell was positioned in the sample compartment of an FTIR spectrometer (Nicolet 6700, Thermo Fisher).

Gas mixtures flow directly through this cell to characterize the dissociation rate of reactants and the formation of major products. However, the concentration of minor products is too low relative to the instrument's thresholds to allow their identification. To overcome this limit, we use a cold trapping strategy to concentrate our products before IR identification. A glass trap installed at the outlet of the system is immersed in liquid nitrogen (78 K) (see Figure 1), ensuring the entire flow passes through it, condensing most of the gases. H_2, CH_4 and CO, with condensation temperatures below 78 K, are not trapped, which helps to concentrate minor products. However, precise quantification is not possible due to this bias-inducing differentiated condensation, but robust product identification is already an important step forward. The irradiated gas stream is allowed to pass through the trap for 20 min; trapping is then stopped, the trap is heated to sublimate the condensed species, the gases are released into the multipass cell, and heated to 70°C so that water vapor does not condense on the mirrors. The pressure is measured inside the cell and it does not exceed a few millibars. Since there is no longer any irradiation, we remain at low pressure and do not reach very high temperatures, so we expect the kinetics to be slow and no significant new reactions to occur. Infrared spectra are measured through the software OMNIC (Thermo Scientific), with a resolution of 0.5 cm^{-1} using the Graymann-Harris apodization function (Harris 1978). 150 scans were accumulated for each measurement, averaged, and combined into a spectrum.

Preprocessing the spectra, using OMNIC software, transforms the single-beam data acquired into transmittance or absorbance spectra, by dividing them by blank spectra previously acquired under high vacuum conditions (less than 10^{-5} mbar) and by applying a manual baseline correction. The IR spectra were compared with those calculated at the experimental pressure (1 mbar) and temperature (340 K), based on the opacities of several species (Figure A.2). The opacities are taken from the databases DACE[2] and HITRAN (Gordon et al. 2017). However, these identifications were limited by the availability of molecules – organic compounds with three or more carbon atoms are not included. For more complex molecules, identification is performed using the NIST database, but this does not allow for temperature and pressure dependence to be taken into account.

2.5. Atmospheric numerical simulations

To model the chemistry occurring in the reactor chamber, we used the 0D photochemical model *ReactorUI* (Peng et al. 2014; Pernot 2023), as described in Peng et al. (2014). This complementary approach to experimental characterization helps to identify the species produced and to elucidate the main chemical pathways leading to their formation (Bourgalais et al. 2020).

The model reproduces experimental conditions, taking into account chamber geometry, gas flows and the distribution of incoming plasma energy, which has been approximated using solar spectra. This is a significant assumption that can influence abundance but still allows pathways to be identified. After adjusting all the parameters, the integration system converges to a steady state.

The chemical network was originally developed for the CHN atmosphere of Titan with neutral-neutral reactions (Hébrard et al. 2007, 2009; Dobrijevic et al. 2016), ions (Carrasco et al. 2008; Plessis et al. 2012) and photo-processes (from the Leiden (Heays et al. 2017) and SWRI (Huebner & Mukherjee 2015) databases). For the studies of the formation of more complex oxygenated molecules, such as H_2CO and CH_3OH, we extended the chemical network with that of CHO *VULCAN* (Tsai et al. 2021), specific to sub-Neptunes, based on Venot et al. (2020).

Simulations of each experimental composition were run. Considering chemical rate uncertainties with a Monte Carlo approach, we perform 500 runs for each configuration. This Monte Carlo approach to characterizing uncertainties has already been used in several atmospheric models of Solar System objects, such as Triton (250 runs, Benne et al. 2022), Titan (500 runs, Hébrard et al. 2009) or Neptune (1000 runs, Dobrijevic et al. 2010). As a result, we evaluate the final species abundance values with its uncertainty. These simulations also provide information on the contributions of specific reactions to the formation or consumption of a given molecule, enabling reaction paths to be extracted.

3. Results

3.1. Identification of main compounds

Table A.1 details the value of the main IR and MS features of the major products. Figure A.2 shows the reference IR spectra extracted from the HITRAN database for the molecules containing up to two carbon atoms considered in this study.

3.1.1. Reduced organic compounds

We observe the formation of reduced organic compounds, composed only of carbon and hydrogen atoms, forming chains with up to six carbon atoms. In MS, groups of peaks form at m/z up to 80 when a 95% H_2 + 5% CH_4 gas mixture is irradiated (Figure 2). The specific fragmentation patterns (FP) of reduced compounds with two and three carbon atoms (C2 and C3) are shown in Figure A.1. These patterns are normalized to the mass spectrum measured in the irradiated gas mixture of 95% H_2 + 5% CH_4, and directly compared with the corresponding mass spectrum. In the case of reduced atmospheres, C2 identification using MS alone is possible, particularly for C_2H_2 and C_2H_6, which exhibit strong characteristic peaks. Infrared spectroscopy is used to determine the nature of the chemical bonds between carbon atoms, distinguishing between single, double and triple bonds. The IR features used to identify acetylene (C_2H_2), ethene (C_2H_4), propyne (C_3H_4) and propene (C_3H_6) are shown in Figure 3.

3.1.2. Oxidized organic compounds

Using IR, we could see in CO and CO_2-rich mixtures the robust formation of the oxidized organic compounds methanol (CH_3OH), formaldehyde (H_2CO) and acetaldehyde (CH_3CHO). The features used for their identification are shown in Figure 4, at 1033 cm^{-1} (9.68 µm) for CH_3OH and at 1745 cm^{-1} (5.73 µm) for the aldehydes (H_2CO and CH_3CHO). In MS, the production of CH_3OH is identified by the appearance of the characteristic peaks at m/z 31 and 32. The fragmentation patterns of H_2CO and

[2] https://dace.unige.ch/opacityDatabase/?

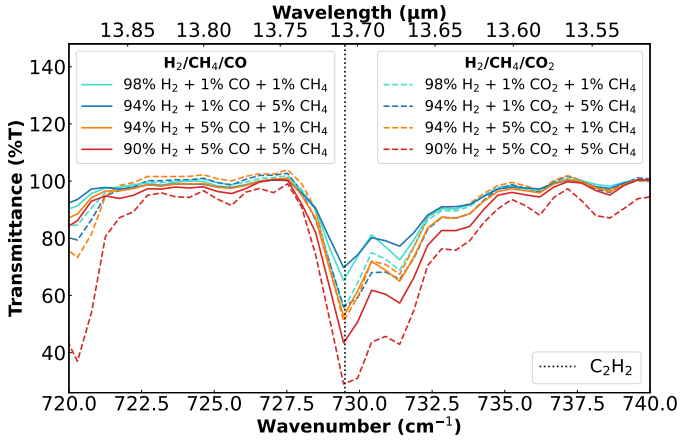

(a) Infrared feature at 730 cm^{-1}(13.70 μm), attributed to C_2H_2.

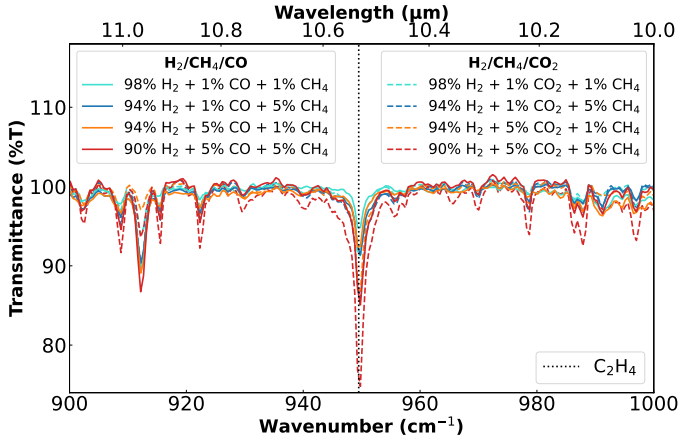

(b) Infrared feature at 950 cm^{-1}(10.53 μm), attributed to C_2H_4.

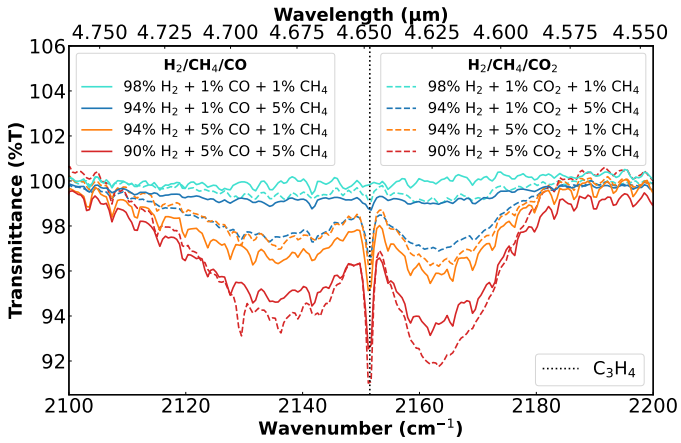

(c) Infrared feature at 2150 cm^{-1}(4.65 μm), attributed to C_3H_4.

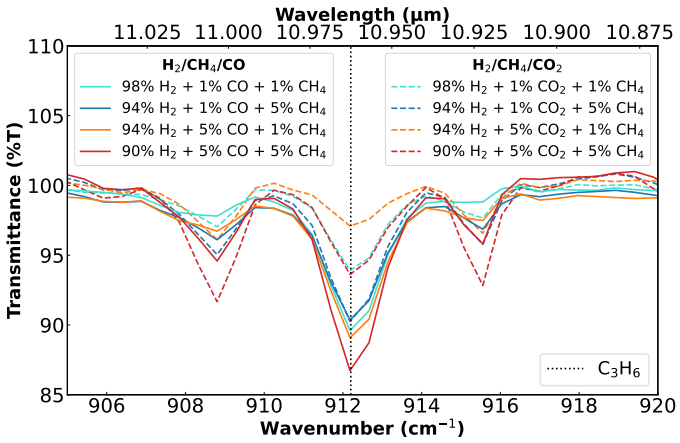

(d) Infrared feature at 912 cm^{-1}(10.96 μm), attributed to C_3H_6.

Fig. 3. Infrared features of the reduced organics.

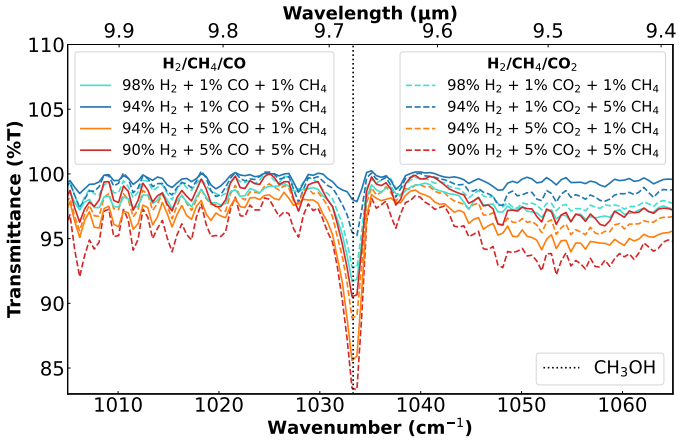

(a) Infrared feature at 1033 cm^{-1}(9.68 μm), attributed to CH_3OH.

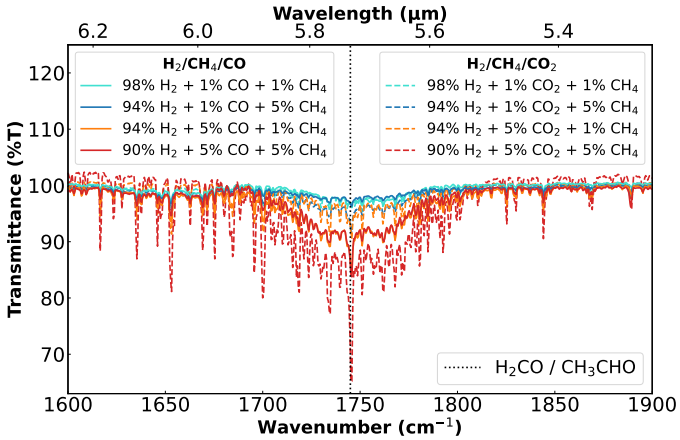

(b) Infrared feature at 1745 cm^{-1}(5.73 μm), attributed to aldehydes.

Fig. 4. Infrared features of the oxidized organics.

CH_3CHO overlap with those of C_2H_6 and C_3H_6, which makes their identification only through MS a source of uncertainty.

3.1.3. Other oxidized compounds

Depending on the degree of oxidation of the reactants, the formation of other oxidized molecules is identified. H_2O is identified in MS with peaks at m/z 17 and 18, and presents wide features in IR. CO is identified with a specific peak at m/z 28 in MS, but is not trapped for IR measurements as discussed in Section 2.4. CO_2 is identified in MS with a peak at m/z 44, and in IR with a narrow peak at 668 cm^{-1}(14.97 μm) and a broad one from 2200 to 2400 cm^{-1}(4.17–4.55 μm).

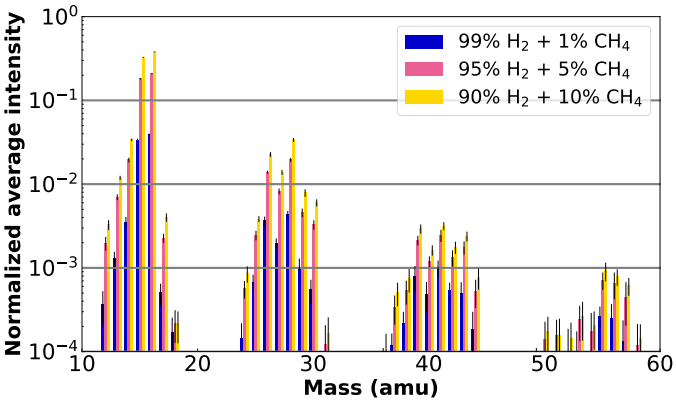

(a) $H_2 + CH_4$

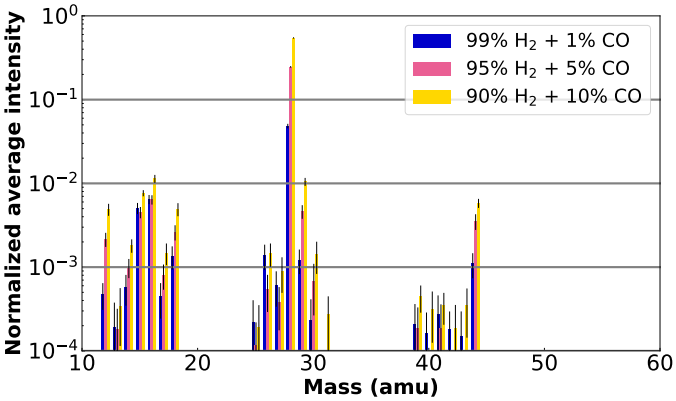

(b) $H_2 + CO$

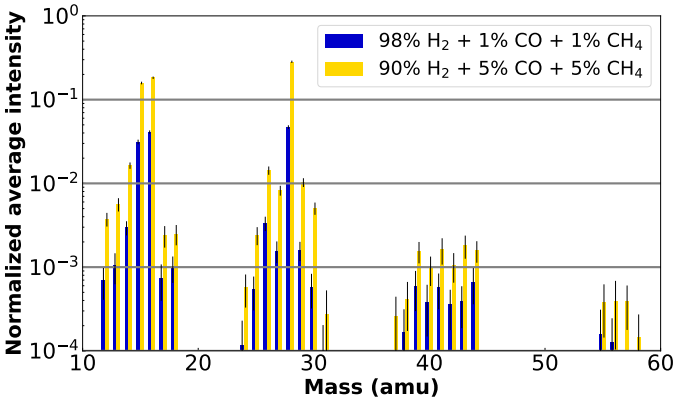

(c) $H_2 + CH_4 + CO$

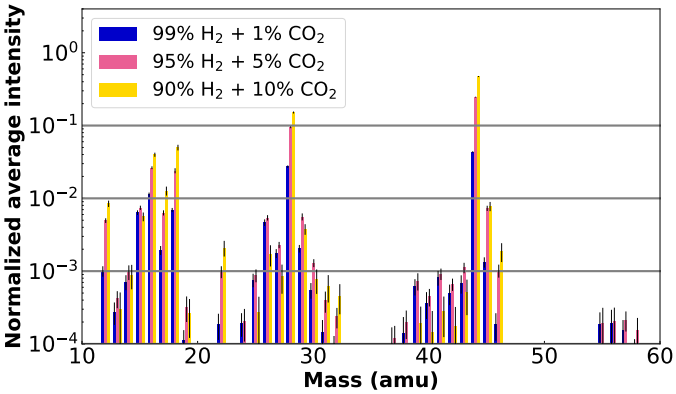

(d) $H_2 + CO_2$

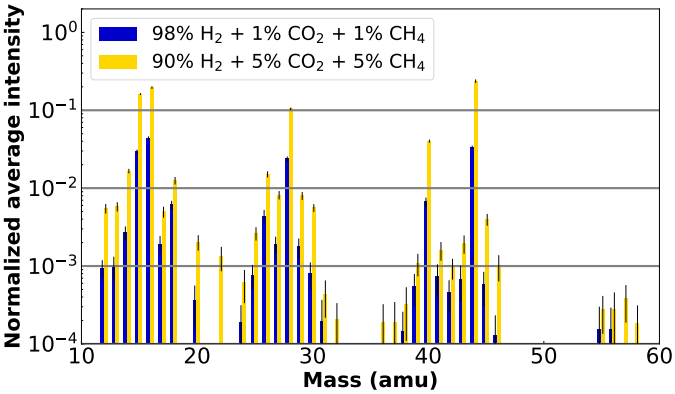

(e) $H_2 + CH_4 + CO_2$

Fig. 5. Mass spectra acquired for different gas mixtures while plasma is ON.

3.2. Abundance and formation trends

3.2.1. Reduced organic compounds

The formation of reduced organics is observed under all experimental conditions. We noted the appearance of carbon chain features both in MS and IR as presented in Section 3.1, shown in Figures 2 and 3, and detailed in Table A.1.

The organic growth is most significant in reduced mixtures, and it increases with methane concentration and hence with metallicity, as expected and already highlighted by previous experimental studies (Hörst et al. 2018). The mass spectra show an increase in the intensity of all peaks with increasing methane content, as shown in Figure 5a. We observed peak groups characteristic of compounds comprising up to four carbon atoms (C4), at m/z 50–60. Although it is difficult to quantify the species precisely, the relative intensities of the peaks relating to C2 compounds appear to be of comparable magnitudes, reflecting similar concentrations. Based on the 0D simulations performed with ReactorUI, we observe that the abundance of C_2H_2 is approximately two orders of magnitude lower than that of C_2H_4 and C_2H_6, and decreases with increasing CH_4 concentration (Figure 6a). In contrast, the abundance of C_2H_4 and C_2H_6 increase with increasing methane concentration.

The formation of reduced organics also occurs in oxidized mixtures, although it is more limited than in reduced mixtures, as previously highlighted in particular for CO_2-rich mixtures (Trainer et al. 2004). It is observed in MS, as we find lower intensities of C2 (m/z 20–30) and C3 (m/z 30–40) specific peak

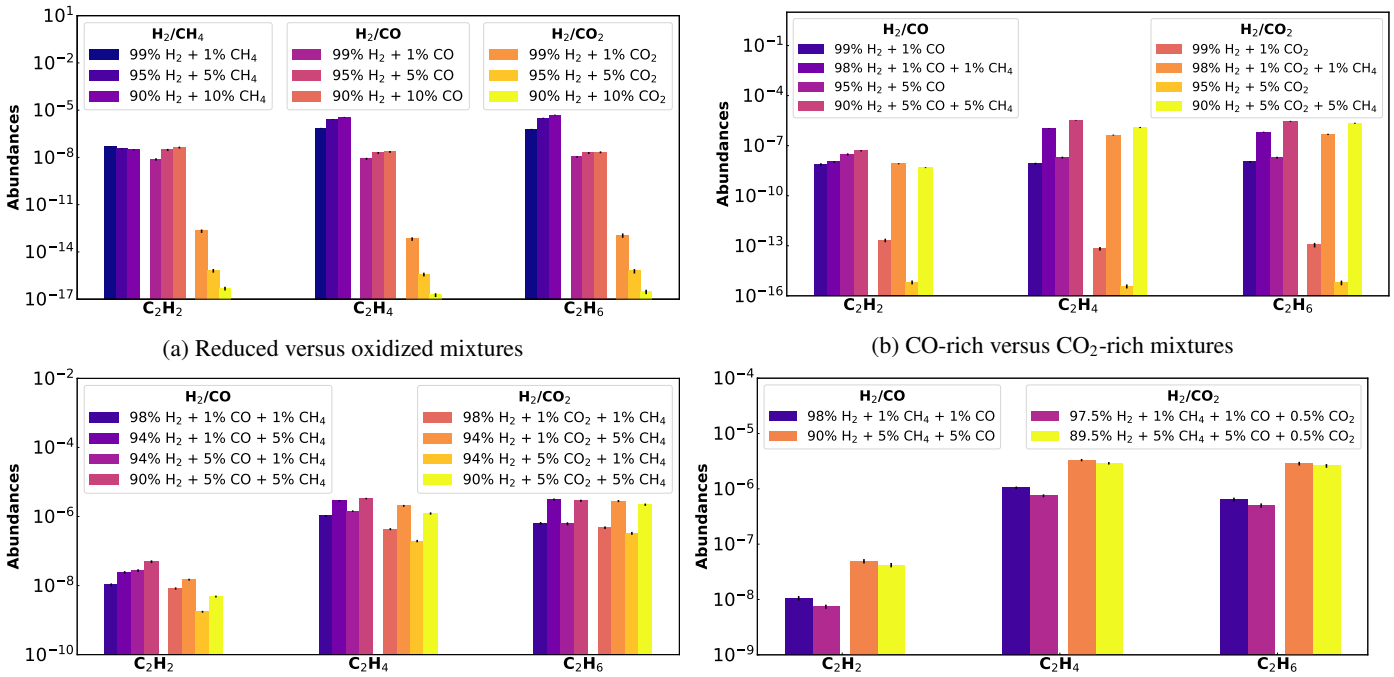

(a) Reduced versus oxidized mixtures

(b) CO-rich versus CO_2-rich mixtures

(c) CH_4/CO versus CH_4/CO_2 mixtures

(d) CH_4/CO versus CH_4/CO/CO_2 mixtures

Fig. 6. Predicted abundance values with 0D simulations of the two-carbon atoms reduced organics in the different gas mixtures.

groups in CO and CO_2-rich mixtures (Figures 5b and 5d) than in reduced mixtures (Figure 5a). In Figures 5b and 5d, we do not observe the C4 specific peak groups at m/z 50–60 that were present in Figure 5a, reflecting inhibited organic growth. No selectivity is observed in oxidized mixtures between the C2 compounds, with simulated abundance values similar for C_2H_2, C_2H_4 and C_2H_6 (Figures 6a, 6b).

The organic growth is predicted by the 0D-simulations to be more efficient with CO-rich mixtures than with CO_2-rich mixtures, as shown in Figure 6a where we see that the abundance values of two-carbon chains are higher with CO than with CO_2. This is not obvious with the MS results presented in Figures 5b and 5d, where we see similar relative intensities of the characteristic m/z ratios of compounds C2 and C3. However this is supported by the IR data, as we observe the appearance of species absorption peaks of three-carbon chains only in CO-rich mixtures (CO and CH_4/CO mixtures). For example, we only see the 912 cm^{-1}(10.96 µm) peak attributed to C_3H_6 clearly appearing in CH_4/CO mixtures, as shown in Figure 3d (solid lines).

For CO-rich mixtures, the organic growth increases with CO concentration. This trend is apparent in the mass spectra in Figure 5b, where we see the intensities of the C2 and C3 peaks increase with CO concentration. This is confirmed by the 0D simulations performed with ReactorUI, as shown in Figure 6a. The predicted abundance of the C2 compounds is higher at a concentration of 10% of CO than at a concentration of 1%.

For CO_2-rich mixtures, this trend is reversed: the organic growth is limited at higher CO_2 concentrations. In the mass spectra, the decrease in the m/z 26 peak – characteristic of C_2H_2, at a CO_2 concentration of 10% – reflects this limitation. The 0D simulations support this trend, with the predicted abundance values of C2 compounds being higher at a concentration of 1% CO_2 than at a concentration of 10%, as shown in Figure 6a.

When H_2, CH_4 and an oxidized compound – CO or CO_2 – are merged, the efficiency of organic growth is a hybrid of the two previous cases. It is increased compared to pure oxidized mixtures, and slightly decreased compared to pure reduced mixtures. In the mass spectra, characteristic peak groups of compounds C2 and C3 are seen in Figures 5c and 5e, at higher intensities than in the oxidized mixtures presented above, but lower than in the reduced mixtures. Figure 6b shows the effect of adding methane to the atmospheres, particularly for the formation of C_2H_4 and C_2H_6: the gain is two to six orders of magnitude, selectively favoring the formation of C_2H_4 and C_2H_6 over C_2H_2. The more oxidized the composite atmosphere is, the less efficient the formation of reduced organics is. This relationship is visible in Figure 6c, where the predicted abundance values for the 94% H_2 + 5% [CO or CO_2] + 1% CH_4 mixtures are the lowest. We also observe in Figure 6d that when 0.5% CO_2 is added to CH_4/CO mixtures, the reduced organics abundance values decrease.

3.2.2. Oxidized organic compounds

The formation of the oxidized organic compounds methanol, formaldehyde and acetaldehyde is identified through IR features shown in Figure 4, only in the atmospheres with CO or CO_2. The trapping method, which concentrates the products so that they can be seen in IR, induces a bias that prevents robust quantification directly from the IR results. However, the 0D model allows us to extract trends for the abundance of these oxidized organic compounds, as a function of gas mixtures, shown in Figure 7.

Figure 7a shows that the relative abundance values of the three oxidized compounds for CO-rich mixtures are always higher than for CO_2-rich mixtures. It also highlights that the growth of these compounds is limited with higher concentrations of CO_2, while it is enhanced with high concentrations of CO. The most abundant oxidized organic product observed with 0D simulations is H_2CO (Figure 7). It is produced in the same abundance range as reduced organic compounds such as C_2H_4 and C_2H_6, and even above the abundance of C_2H_2 (Figure 6c). CH_3OH is much less produced – below the ppb range.

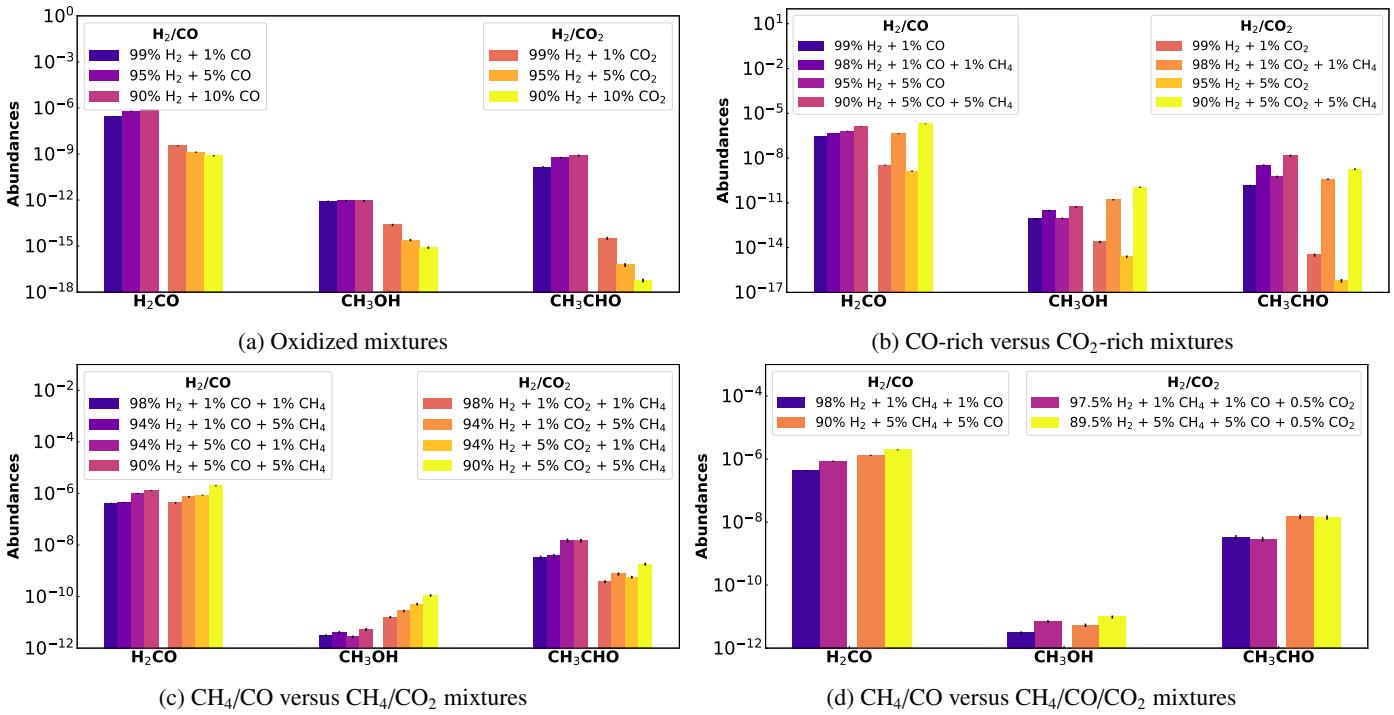

(a) Oxidized mixtures

(b) CO-rich versus CO_2-rich mixtures

(c) CH_4/CO versus CH_4/CO_2 mixtures

(d) CH_4/CO versus CH_4/CO/CO_2 mixtures

Fig. 7. Predicted abundance values with 0D simulations of the oxidized organics in the different gas mixtures.

When CH_4 is added to the atmosphere, the production of oxidized organics is significantly increased (Figure 7b), and enhanced at higher concentrations of both CO and CO_2. In this case, we observe that the formation of H_2CO and CH_3OH becomes more efficient with CO_2 than with CO. We observe in Figure 4 that for a given concentration (same color), the intensity of the feature always appears to be greater in $H_2/CH_4/CO_2$ mixtures (dotted lines) than in H_2/CH_4/CO mixtures (solid lines). This is confirmed by the results of the 0D simulations, where higher abundance values for H_2CO and CH_3OH are observed in CO_2-rich mixtures than in those that are CO-rich (Figure 7c). On the other hand, the abundance values of CH_3CHO remains higher with CO than with CO_2. The combination of CH_4, CO and CO_2 increases the abundance of all oxidized organics of about one order of magnitude (Figure 7d).

3.3. Formation mechanisms

From the 0D simulations performed with ReactorUI, we can determine the key reactions involved in the production and destruction of each chemical compound. This allows us to reconstruct the chemical networks involving the molecules that interest us in our study.

3.3.1. Reduced organic compounds

Figure 8a shows the formation pathway of the C2 compounds from the reactant CH_4 in reduced mixtures. From the dissociation of CH_4, several intermediates are produced, which recombined to form the C2 compounds. C_2H_6 is mainly formed by the combination reaction of 2 CH_3 compounds, C_2H_4 is mainly produced by the reaction of CH with CH_4, and C_2H_2 mainly comes from the combination of two triplet methylene radicals $^3CH_2$. The radical reaction required for the production of C_2H_2 – which is approximately three orders of magnitude slower than the combination reactions forming C_2H_4 and C_2H_6 – could explain its lower abundance predicted by 0D simulations. The relative contributions of these reactions in the formation of the reduced organics remains more or less the same as the concentration of CH_4 increases. That is coherent with the fact that the higher the proportion of CH_4 in the atmosphere – and therefore the higher the metallicity – the higher the final concentrations of reduced organic compounds.

This chemical reaction network (Figure 8a) is consistent with the well-known methane chemistry and hydrocarbon formation studied in the reduced atmospheres of our Solar System, such as Titan (Nixon 2024), Jupiter (Moses et al. 2005) or Saturn (Moses et al. 2000), as well as with predictions made for exoplanets with H_2 dominant atmospheres (Adams et al. 2022). This validates our approach, and gives us confidence for the study of our more oxidized atmospheric ranges.

Figure 8b shows the formation pathway of reduced organics from CO and CO_2. Organic growth is inhibited compared to reduced mixtures, as has been previously studied in the literature – particularly in the CO_2 case by Trainer et al. (2004). It requires passing through more intermediates than in the reduced atmospheres, which limits the formation of reduced organic compounds. The formation of C_2H_4 and C_2H_6 requires the prior formation of the CH_3 intermediate, which in turn is produced by two consecutive intermediates (C and $^3CH_2$) after CO dissociation. This long reaction path explains the lower abundance of hydrocarbons compared to the reduced atmosphere. Furthermore, the dissociation of CO, which provides a source of carbon atoms for organic growth, is at the same time a source of exited oxygen radicals, mainly in the $O(^3P)$ state, which will oxidize some of the carbonate radical intermediates and reduced organics (Figure 9). For example, $^3CH_2$ reacts with $O(^3P)$ to reform CO. However, as the concentration of CO in gas mixtures increases, there is an overall rise in the formation of reduced organic compounds, showing that with CO, the effect of increasing the carbon source dominates over the loss of intermediates by oxidation for the formation of the organics.

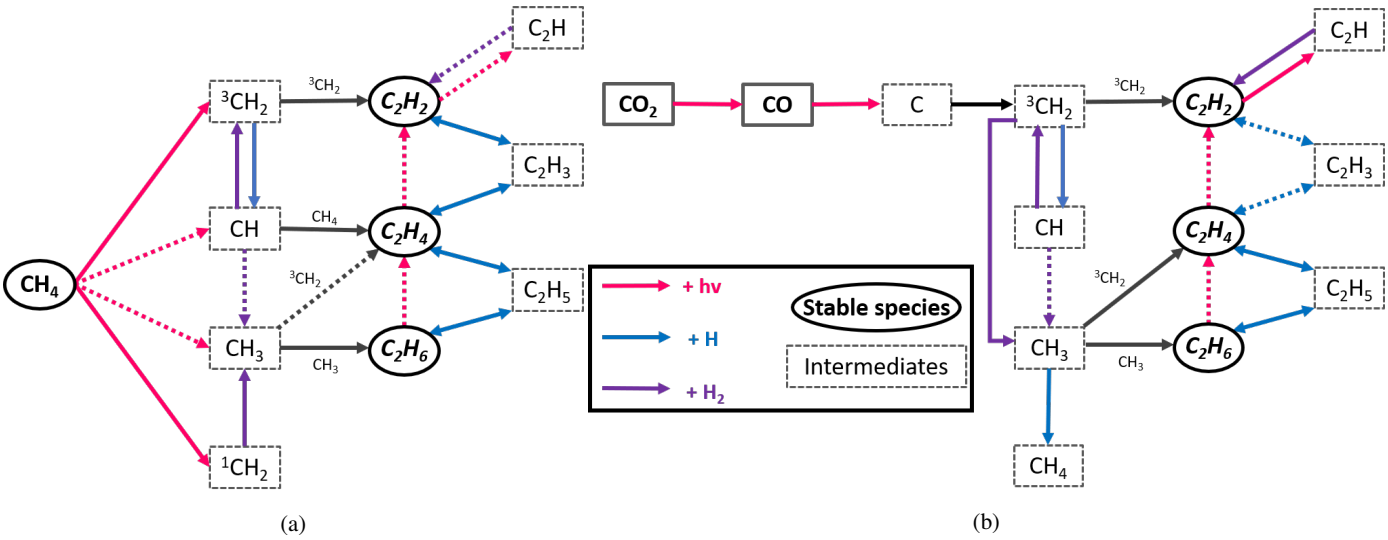

Fig. 8. Formation pathways of reduced organics with main (solid arrows) and minor (dotted arrows) reactions started from a reduced reactant (CH_4, panel a) or an oxidized one (CO or CO_2, panel b).

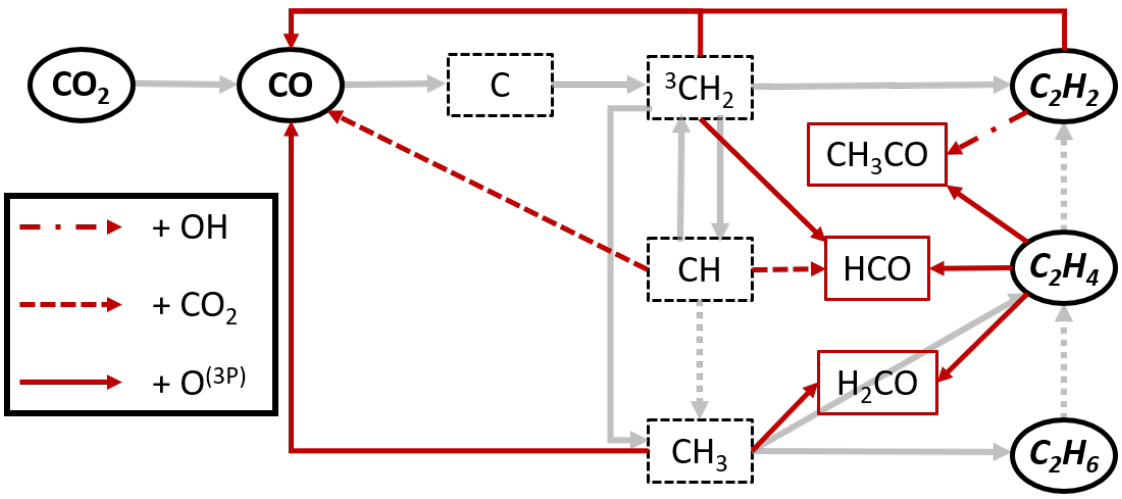

Fig. 9. Main pathways of loss through oxidation of reduced organic compounds (red) superimposed on their formation pathways (light gray) presented in Figure 8b.

For CO_2-rich mixtures, the difference in efficiency in the formation of reduced organic compounds compared to CO-rich mixtures can be linked with the fact that it first requires the dissociation of CO_2 before producing the intermediates. This produces CO and an exited oxygen radical, mainly in the $O(^1D)$ state. The conversion of CO_2 into CO is not total, which explains why the source of carbon is less abundant than in the case where CO is a reactant. In addition, the production of oxygen radicals is doubled, as a first radical is produced from the dissociation of CO_2 and a second from the dissociation of CO. The oxidation of carbonate intermediates and reduced organics is more important. For example, the reaction of C_2H_2 with OH radical, which is a minor loss reaction in the case of CO, becomes dominant in the case of CO_2. This is related to the fact that the formation of OH radicals is more efficient from CO_2 than from CO, thanks to the following combination reaction, which is an order of magnitude faster with CO_2 than with CO:

$$O^1D + H_2 \longrightarrow OH + H. \quad (1)$$

The main pathways of loss through oxidation are shown in Figure 9. These combined effects explain why the abundance of reduced organic substances in CO_2-rich gas mixtures is much lower than in CO-rich mixtures, and why the abundance of reduced organic compounds decreases with increasing CO_2.

As CH_4 is a reactant in the $CH_4/CO/CO_2$ mixtures, the reaction pathway presented in Figure 8a also explains the organic growth. When atmospheres are more oxidized, we can observe the same mechanisms that are distinctive of fully oxidized atmospheres, as developed in Figure 8b, but with a limitation in organic growth due to the oxidation of reaction products and intermediates.

In summary, organic growth efficiency is best in CH_4-rich mixtures, as expected, and is significant in oxidized mixtures, although more limited. In mixtures rich in CO_2, oxidative loss reactions become predominant and limit hydrocarbon formation, even at high metallicity values. In CO-rich mixtures, the effect of the carbon source partially compensates for the inhibitory effect of the oxygen source, and we observe that organic growth efficiency increases with metallicity, as in reduced gas mixtures.

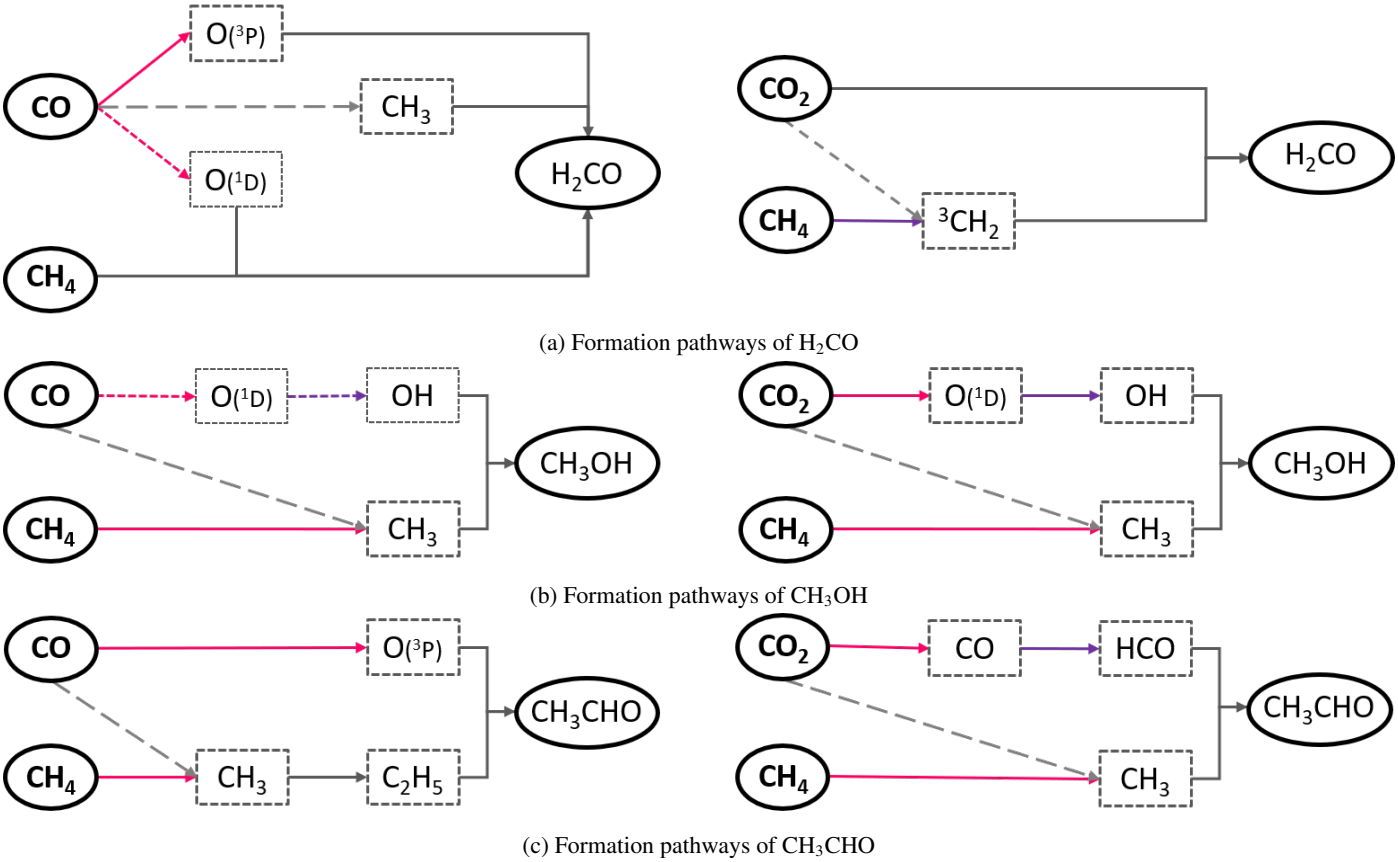

Fig. 10. Formation pathways of oxidized organics. The formation pathways of the intermediates CH_3 and $^3CH_2$ from CO or CO_2 are detailed in Figure 8 and are simplified here by long dotted gray arrows. The main (solid arrows) and minor (short dotted arrows) reactions are represented.

3.3.2. Oxidized organic compounds

The main formation pathways of H_2CO and CH_3CHO are different depending on the oxidized reactant, as shown in Figures 10a and 10c, while for CH_3OH it is similar for CO and CO_2. All these reaction paths involve reduced organic intermediates, such as CH_3 and $^3CH_2$, for which the formation efficiency in CO or CO_2 mixtures is described in Section 3.2.1. This explains the formation trends observed, i.e., formation efficiency is better with CO than with CO_2, enhanced at high CO concentrations and limited at high CO_2 concentrations. The formation of CH_3OH and CH_3CHO in mixtures of CO and CO_2 requires at least one more intermediate than the formation of H_2CO. This makes the formation of H_2CO up to six orders of magnitude faster, explaining its predominance.

The main loss pathways of oxidized organic compounds could provide an additional explanation for the predominance of H_2CO over CH_3OH and CH_3CHO. Indeed, in all gas mixtures, the loss of H_2CO is mainly due to the following reactions:

$$H_2CO + H \longrightarrow HCO + H \tag{2}$$

$$H_2CO + h\nu \longrightarrow CO + H_2. \tag{3}$$

The reaction of H_2CO with H is almost two orders of magnitude faster than its photodissociation in the 0D model. HCO and CO are themselves involved as reactants in the formation of H_2CO. In this way, H_2CO is self-sustaining, which explains its high abundance. In contrast, CH_3OH can be photo-dissociated through

$$CH_3OH + h\nu \longrightarrow H_2CO + H_2, \tag{4}$$

which forms H_2CO again.

The addition of CH_4 in the gaseous mixture enhances all the productions, since the formation pathways of the reduced intermediates are much shorter starting from the reactant CH_4 than from CO or CO_2. With this limiting effect removed, the production of H_2CO and CH_3OH from CO_2 is more efficient than with CO. This is because CO_2 is a direct reactant in the formation of H_2CO, whereas with CO, the intermediate $O(^1D)$ is required (Figure 10a), which is a minor product during the dissociation of CO. For the formation of CH_3OH, the same reaction pathway is followed from CO or from CO_2 (Figure 10b), requiring the intermediate $O(^1D)$, a major product during the dissociation of CO_2. However, since the formation of CH_3CHO from CO_2 requires one more intermediate than from CO (Figure 10c), it remains more efficient with CO than with CO_2.

In summary, the efficiency of the formation of oxidized organic compounds is greater in H_2/CO mixtures and increases with metallicity. In H_2/CO_2 mixtures, formation of oxidized organic compounds is limited and decreases with the metallicity. However, the combination of CH_4 with CO or CO_2 significantly increases the formation of oxidized products, in correlation with metallicity. The efficiency of H_2CO and CH_3OH formation is therefore higher in CH_4/CO_2 mixtures than in CH_4/CO mixtures.

4. Discussion

4.1. Roles of methane, carbon monoxide, and carbon dioxide in organic growth

Methane plays a predominant role in organic growth, as demonstrated in our experiments, in which we observed a positive correlation between gas-phase hydrocarbon production and methane concentration. This is consistent with previous experiments in the literature, which have highlighted the major role of methane in the growth of solid particles (tholins) when N_2/CH_4 Titan-type mixtures are irradiated (Hörst & Tolbert 2013; Hörst et al. 2018; Moran et al. 2022; Jovanović et al. 2020; Jovanovic 2021). The production of the solid phase in Titan-type mixtures is optimized between 3 and 5% of CH_4 (Sciamma-O'Brien et al. 2010). In this study, in H_2-dominated mixtures up to 10% of CH_4, we observe continuous growth of hydrocarbons in the gas phase, without an obvious optimal concentration. This optimum would possibly occur at higher proportions of CH_4.

While methane is clearly identified as a major driver of organic growth, the effect of oxidized reactants is not as clearly correlated. At first glance, we identified an inhibitory effect due to the atomic oxygen source represented by the oxidized reactants, thus limiting the growth of long carbon chains. This is even more pronounced with CO_2, which provides twice as much oxygen. This effect has also been identified in the production of solid particles in N_2/CH_4 mixtures, where the addition of CO alters the kinetics of methane, delaying the appearance of solid particles and reducing their production rate (Fleury et al. 2014; He et al. 2017; Moran et al. 2022).

However, CO and CO_2 are also sources of carbon and can contribute to organic growth. Trainer et al. (2006) showed that adding CO_2 to a N_2/CH_4 mixture could increase particle production up to a CH_4/CO_2 ratio of 1 before decreasing. This effect is particularly evident in our CH_4-free mixtures, where hydrocarbon production is still observed, although at lower levels than in the case where CH_4 is present. The addition of CO to N_2/CH_4 mixtures, although reducing the production rate of tholins, increases their size (Fleury et al. 2014; Hörst & Tolbert 2014). In our study, we observe a positive correlation between the formation of organic compounds in the gas phase and the concentration of CO. That highlights that with CO, the effect of increasing the carbon source dominates over the loss by oxidation. In the case of a low methane concentration (1%), Jovanović et al. (2020) observed a higher production rate in the presence of 500 ppm CO than in its absence, highlighting the important role that CO can play as a carbon source when methane is less dominant.

Furthermore, the addition of oxygen atoms increases the diversification and organic complexity of photochemical products. We observe the appearance of oxidized organic compounds of prebiotic interest in our CO and CO_2-rich mixtures (CH_3OH, H_2CO, CH_3CHO). It has also been shown that adding CO to Titan-type mixtures improves the reactivity of the gas phase (Yang et al. 2025; Fleury et al. 2014), leading to the incorporation of oxygen in both the gas and solid phases (He et al. 2017). Similarly, the addition of CO_2 leads to more oxidized solid compounds (Trainer et al. 2004). Since CO_2 is a more important source of oxygen than CO, one would expect oxygen incorporation to be better. In our study, this corresponds to the observation that oxidized organic compounds are better produced in the gas phase with CO_2 than with CO when combined with CH_4 and therefore when organic growth is not too limited. For the solid phase, Drant et al. (2026) observed in N_2/CH_4-rich exoplanetary haze analogs that the characteristic absorption bands of oxygenated functions (O–H, C=O) are clearly visible in analogs produced with CO_2, but not or only very weakly in those produced with CO alone.

4.2. Photochemistry of hydrocarbons in temperate methane-rich exoplanet atmosphere

Experiments conducted in reduced gas mixtures reveal similar formation rates for C2 compounds, preventing any definitive conclusions about selectivity. Simulated abundance using the 0D model also predicts comparable values for these molecules, but with a slight selectivity observed for C_2H_6 and C_2H_4 relative to C_2H_2. This contrasts with the hydrocarbon photochemistry observed in the gas giants Jupiter and Saturn, where detected abundance is depleted in C_2H_4 and enriched in C_2H_6 and C_2H_2 (Moses et al. 2000, 2005; Nixon et al. 2010). These planets have hydrogen-dominated atmospheres with significant helium concentrations and a small fraction of methane (around 0.1%). They are cooler – around 150 K at 1 mbar.

The low abundance of C_2H_4 is explained by its high photodissociation rate at Lyman-α, producing C_2H_2, and by its reaction with H, which recycles it into CH_4 (Gladstone et al. 1996). In contrast, C_2H_6 is shielded by methane and thus remains stable at Lyman-α. In our study, the energy distribution of electrons in our plasma covers a much wider range than that of photons in planetary atmospheres, which are largely concentrated around Lyman-α. Consequently, the wavelength selectivity of photodissociation is not reproduced, which likely contributes to the differences observed in the relative abundance of C2 compounds between our experiments and planetary atmospheres.

Additionally, C_2H_2, as a highly unsaturated compound, would normally be unstable in an H_2-dominated environment. However, it is efficiently recycled via the recombination reaction

$$C_2H + H_2 \longrightarrow C_2H_2 + H. \tag{5}$$

We noticed that this reaction is negligible in our reduced gas mixtures, whereas it becomes significant in oxidized mixtures. Since CO and CO_2 are sources of carbon but create a less reducing environment than CH_4, this increases the degree of unsaturation of the products. This has also been demonstrated for the production of solid products (He et al. 2017; Yang et al. 2025). This corresponds to the fact that we observe a depletion of C_2H_2 in mixtures containing only CH_4, whereas there is no apparent selectivity in mixtures containing CO and CO_2.

Temperature differences may also play a role in C2 relative abundance. Adams et al. (2022) suggests that warmer H_2-rich atmospheres, compared to Titan, favor dynamic chemical cycles involving C_2H_2, C_2H_3, and C_2H_4 through reactions with atomic hydrogen. These processes can reduce C_2H_6 and C_2H_2 concentrations while increasing the relative abundance of C_2H_4.

4.3. Detectability of photoproducts

4.3.1. Hydrocarbons

The C2 compounds appear to be relatively abundant and efficiently produced in our experiments, which are dominated by out-of-equilibrium chemistry. Similarly, a 1D non-equilibrium chemical model fitting the JWST observational data of K2-18 b predicts that C_2H_2, C_2H_4 and C_2H_6 could reach volume mixing ratios of up to a few percent in the upper atmosphere (at

1 mbar) (Jaziri et al. 2025). C_2H_2 and C_2H_4 are in principle detectable with JWST, using combined observations from the NIRSpec/G395 and MIRI LRS instruments, provided their mixing ratios exceed 10^{-6} (Gasman et al. 2022). This suggests that the detection of hydrocarbons in the atmosphere of K2-18 b is plausible if methane is abundant and predominant over carbon dioxide, as predicted by Wogan et al. (2024); Schmidt et al. (2025); Jaziri et al. (2025); Hu et al. (2025), and if photochemistry is sufficiently active. The 3.4 and 6.9 µm features observed in the NIRSpec and MIRI data could plausibly be attributed to C_2H_6 (Luque et al. 2025), providing an alternative to their attribution to DMS (dimethyl sulfide) or DMDS (dimethyl disulfide) by Madhusudhan et al. (2025). In summary, two-atom hydrocarbons are good candidates for detection with current JWST observations and future high-resolution ground-based observations, both in terms of expected abundance and photochemical plausibility. It is necessary to consider them before considering more complex species with a variety of potential sources.

4.3.2. Oxidized organics

Our complementary experimental approach combining MS and IR spectroscopy enables robust identification of H_2CO, CH_3OH, and CH_3CHO formation in oxidized gas mixtures. Jaziri et al. (2025) predict that H_2CO, CH_3OH, and CH_3CHO could reach volume mixing ratios of up to a few parts per million (10^{-6}) in the upper atmosphere of K2-18 b. However, detectability studies with JWST indicate that species such as H_2CO and CH_3OH require volume mixing ratios exceeding 10^{-5} to produce measurable features in H_2-dominated atmospheres (Huang et al. 2022; Zhan et al. 2022). Their detection in the atmosphere of K2-18 b therefore seems unlikely given current sensitivity limits. Nevertheless, our results suggest that in other H_2-rich exoplanets with a higher CO and/or CO_2 content, the formation of oxidized organic species may be particularly efficient. In such environments, these molecules could form more abundantly and potentially reach detectable levels with JWST or with future high-resolution ground-based instruments on the Extremely Large Telescope (ELT), such as ANDES (ArmazoNes high Dispersion Echelle Spectrograph, Palle et al. 2025) and PCS (Planetary Camera and Spectrograph, Kasper et al. 2021).

5. Conclusion

We studied out-of-equilibrium chemistry in H_2-dominant atmospheres typical of temperate sub-Neptunes by combining experimental and numerical simulations. This approach complements previous laboratory studies by enabling more accurate molecular identification and clearer elucidation of reaction pathways. Our experiments, which are based on the combined use of MS and IR spectroscopy, enabled the reliable detection of reduced (C_2H_2, C_2H_4, C_2H_6) and oxidized (CO, CO_2, H_2O, H_2CO, CH_3OH, CH_3CHO) species in gas mixtures covering a wide range of C/O ratios and metallicities. The use of the 0D photochemical model allowed us to extract abundance trends and identify formation pathways.

Hydrocarbon compounds are produced in methane-rich atmospheres in particular. The efficiency of this organic growth increases with metallicity in CH_4-rich and CO-rich atmospheric analogs. In CO_2-rich atmospheric analogs, oxidative loss reactions become predominant and limit the formation of hydrocarbons. The formation of hydrocarbons from methane can be explained by reaction pathways that have already been well studied in the atmospheres of the Solar System, whereas their formation from oxidized reactants – CO or CO_2 – involves more reaction intermediates and a change in the predominance of certain pathways. This explains the lower abundance of reduced organic compounds in an oxidized atmosphere, combined with the emergence of oxidation pathways that consume reaction intermediates, which have more influence for low C/O ratios. The addition of oxygen diversifies the chemistry, and in CO-rich and CO_2-rich mixtures in particular, it leads to the formation of the oxidized organic compounds presented above. The combination of CH_4 and CO has a twofold effect. On the one hand, it provides carbon-rich atmospheres, which promote the efficient formation of hydrocarbons. On the other hand, it leads to moderately oxygenated atmospheres, which promote the formation of oxidized organic compounds without overly enhancing the pathways for hydrocarbon destruction.

Our study highlights the importance of adopting a synergistic approach combining experiments, modeling, and observations in order to deepen our understanding of exoplanet atmospheres. Each field offers unique perspectives, but through close collaboration their potential is greatly enhanced, and therefore strengthening these interdisciplinary efforts is essential.

6. Perspectives

The gas mixtures studied here cover a wide range of potential atmospheres. However, these are still fairly simple mixtures at a fixed temperature, which do not cover all possible atmospheric compositions of exoplanets. For example, the effect of temperature, other oxygen-containing reactants such as water in higher proportions, nitrogenous species, sulfur species, could be studied in the future. It would be very useful to study the detectability of photoproducts in detail, both for JWST observations and for future high-resolution ground-based observations.

Data availability

Mass spectra, IR spectra, and 0D model data can be downloaded from Zenodo: https://doi.org/10.5281/zenodo.17868179

Acknowledgements. This project has received funding from the European Research Council (ERC) under the ERC OxyPlanets projects (grant agreement No. 101053033). We would like to thank the anonymous referee for their excellent comments, which improved the presentation of our results. The authors thank Olivier Guaitella for kindly lending the multipass infrared cell, which was essential for this work. We would like to extend our warmest thanks to Joleen Csuka and Elisha Wesley Belibio for their valuable and helpful advice on proofreading and copyediting.

References

Adams, D., Luo, Y., & Yung, Y. L. 2022, Front. Astron. Space Sci., 9, 823227
Benne, B., Dobrijevic, M., Cavalié, T., Loison, J.-C., & Hickson, K. M. 2022, A&A, 667, A169
Benneke, B., Roy, P.-A., Coulombe, L.-P., et al. 2024, arXiv e-prints [arXiv:2403.03325]
Bourgalais, J., Carrasco, N., Changeat, Q., et al. 2020, ApJ, 895, 77
Bourgalais, J., Carrasco, N., Miguel, Y., Venot, O., & Pernot, P. 2021, A&A, 654, A171
Brande, J., Crossfield, I. J. M., Kreidberg, L., et al. 2024, ApJ, 961, L23
Butlerow, A. 1861, Justus Liebigs Ann. Chem., 120, 295
Cabot, S. H. C., Madhusudhan, N., Constantinou, S., et al. 2024, ApJ, 966, L10
Carrasco, N., Alcaraz, C., Dutuit, O., et al. 2008, Planet. Space Sci., 56, 1644
Carrasco, N., Gautier, T., Es-sebbar, E.-t., Pernot, P., & Cernogora, G. 2012, Icarus, 219, 230

Charnay, B., Blain, D., Bézard, B., et al. 2021, A&A, 646, A171
Cleaves, II, H. J. 2008, Precamb. Res., 164, 111
Dobrijevic, M., Cavalié, T., Hébrard, E., et al. 2010, Planet. Space Sci., 58, 1555
Dobrijevic, M., Loison, J. C., Hickson, K. M., & Gronoff, G. 2016, Icarus, 268, 313
Doyon, R. 2024, arXiv e-prints [arXiv:2403.12617]
Drant, T., Sciamma-O'Brien, E., Jovanovic, L., et al. 2026, A&A, 706, A167
Dressing, C. D., & Charbonneau, D. 2015, ApJ, 807, 45
Dubois, D., Carrasco, N., Petrucciani, M., et al. 2019, Icarus, 317, 182
Dubois, D., Carrasco, N., Jovanovic, L., et al. 2020, Icarus, 338, 113437
Espinoza, N., Allen, N. H., Glidden, A., et al. 2025, ApJ, 990, L52
Fleury, B. 2015, PhD thesis, Université Paris-Saclay (ComUE)
Fleury, B., Carrasco, N., Gautier, T., et al. 2014, Icarus, 238, 221
Fleury, B., Carrasco, N., Millan, M., Vettier, L., & Szopa, C. 2017, Earth Planet. Sci. Lett., 479, 34
Fleury, B., Gudipati, M. S., Henderson, B. L., & Swain, M. 2019, ApJ, 871, 158
Fleury, B., Gudipati, M. S., Henderson, B. L., & Swain, M. 2020, ApJ, 899, 147
Fleury, B., Benilan, Y., Venot, O., et al. 2023, ApJ, 956, 134
France, K., Froning, C. S., Linsky, J. L., et al. 2013, ApJ, 763, 149
Fressin, F., Torres, G., Charbonneau, D., et al. 2013, ApJ, 766, 81
Gao, P., Wakeford, H. R., Moran, S. E., & Parmentier, V. 2021, J. Geophys. Res. (Planets), 126, e06655
Gasman, D., Min, M., & Chubb, K. L. 2022, A&A, 659, A114
Gavilan, L., Broch, L., Carrasco, N., Fleury, B., & Vettier, L. 2017, ApJ, 848, L5
Gavilan, L., Carrasco, N., VrOnning Hoffmann, S., Jones, N. C., & Mason, N. J. 2018, ApJ, 861, 110
Gillon, M., Ducrot, E., Bell, T. J., et al. 2025, Nat. Astron., accepted [arXiv:2509.02128]
Gladstone, G. R., Allen, M., & Yung, Y. L. 1996, Icarus, 119, 1
Glidden, A., Ranjan, S., Seager, S., et al. 2025, ApJ, 990, L53
Gordon, I. E., Rothman, L. S., Hill, C., et al. 2017, J. Quant. Spec. Radiat. Transf., 203, 3
Hardegree-Ullman, K. K., Cushing, M. C., Muirhead, P. S., & Christiansen, J. L. 2019, AJ, 158, 75
Harris, F. J. 1978, IEEE Proc., 66, 51
He, C., Hörst, S. M., Riemer, S., et al. 2017, ApJ, 841, L31
He, C., Hörst, S. M., Lewis, N. K., et al. 2018a, AJ, 156, 38
He, C., Hörst, S. M., Lewis, N. K., et al. 2018b, ApJ, 856, L3
He, C., Hörst, S. M., Lewis, N. K., et al. 2019, ACS Earth Space Chem., 3, 39
He, C., Hörst, S. M., Lewis, N. K., et al. 2020, Planet. Sci. J., 1, 51
Heays, A. N., Bosman, A. D., & van Dishoeck, E. F. 2017, A&A, 602, A105
Hébrard, E., Dobrijevic, M., Bénilan, Y., & Raulin, F. 2007, Planet. Space Sci., 55, 1470
Hébrard, E., Dobrijevic, M., Pernot, P., et al. 2009, J. Phys. Chem. A, 113, 11227
Holmberg, M., & Madhusudhan, N. 2024, A&A, 683, L2
Hörst, S. M., & Tolbert, M. A. 2013, ApJ, 770, L10
Hörst, S. M., & Tolbert, M. A. 2014, ApJ, 781, 53
Hörst, S. M., He, C., Lewis, N. K., et al. 2018, Nat. Astron., 2, 303
Hu, R., Bello-Arufe, A., Tokadjian, A., et al. 2025, AAS J., submitted [arXiv:2507.12622]
Huang, J., Seager, S., Petkowski, J. J., Zhan, Z., & Ranjan, S. 2022, ApJ, 933, 6
Huebner, W. F., & Mukherjee, J. 2015, Planet. Space Sci., 106, 11
Jaziri, A. Y., Sohier, O., Venot, O., & Carrasco, N. 2025, A&A, 701, A33
Jiménez-Escobar, A., Ciaravella, A., Mangione, A., et al. 2025, Planet. Sci. J., 6, 135
Jovanovic, L. 2021, PhD thesis, Université Paris-Saclay
Jovanović, L., Gautier, T., Vuitton, V., et al. 2020, Icarus, 346, 113774
Kasper, M., Cerpa Urra, N., Pathak, P., et al. 2021, The Messenger, 182, 38
Linstrom, P., & Mallard, W. 2001, J. Chem. Eng. Data, 46, 1059
Luger, R., & Barnes, R. 2015, Astrobiology, 15, 119
Luque, R., Piaulet-Ghorayeb, C., Radica, M., et al. 2025, A&A, 700, A284
Madhusudhan, N., Sarkar, S., Constantinou, S., et al. 2023, ApJ, 956, L13
Madhusudhan, N., Constantinou, S., Holmberg, M., et al. 2025, ApJ, 983, L40
Mahjoub, A., Carrasco, N., Dahoo, P. R., et al. 2012, Icarus, 221, 670
Mathew, T., Esteves, P. M., & Prakash, G. K. S. 2022, Front. Astron. Space Sci., 9, 809928
Moran, S. E., Hörst, S. M., Vuitton, V., et al. 2020, Planet. Sci. J., 1, 17
Moran, S. E., Hörst, S. M., He, C., et al. 2022, J. Geophys. Res. (Planets), 127, e06984
Morley, C. V., Fortney, J. J., Marley, M. S., et al. 2015, ApJ, 815, 110
Moses, J. I., Bézard, B., Lellouch, E., et al. 2000, Icarus, 143, 244
Moses, J. I., Fouchet, T., Bézard, B., et al. 2005, J. Geophys. Res. (Planets), 110, E08001
Nixon, C. A. 2024, ACS Earth Space Chem., 8, 406
Nixon, C. A., Achterberg, R. K., Romani, P. N., et al. 2010, Planet. Space Sci., 58, 1667
Owen, J. E., & Mohanty, S. 2016, MNRAS, 459, 4088
Palle, E., Biazzo, K., Bolmont, E., et al. 2025, Exp. Astron., 59, 29
Peng, Z., Carrasco, N., & Pernot, P. 2014, GeoResJ, 1, 33
Pernot, P. 2023, ppernot/ReactorUI: Ready for sulfur
Piaulet-Ghorayeb, C., Benneke, B., Turbet, M., et al. 2025, ApJ, 989, 181
Pinto, J. P., Gladstone, G. R., & Yung, Y. L. 1980, Science, 210, 183
Plessis, S., Carrasco, N., Dobrijevic, M., & Pernot, P. 2012, Icarus, 219, 254
Quirico, E., Montagnac, G., Lees, V., et al. 2008, Icarus, 198, 218
Reed, N. W., Shearer, R. L., McGlynn, S. E., et al. 2024, ApJ, 973, L38
Ricker, G. R., Winn, J. N., Vanderspek, R., et al. 2015, J. Astron. Telesc. Instrum. Syst., 1, 014003
Rimmer, P. B., Xu, J., Thompson, S. J., et al. 2018, Sci. Adv., 4, eaar3302
Scalo, J., Kaltenegger, L., Segura, A., et al. 2007, Astrobiology, 7, 85
Schmidt, S. P., MacDonald, R. J., Tsai, S.-M., et al. 2025, AJ, accepted [arXiv:2501.18477]
Sciamma-O'Brien, E., Carrasco, N., Szopa, C., Buch, A., & Cernogora, G. 2010, Icarus, 209, 704
Shields, A. L., Ballard, S., & Johnson, J. A. 2016, Phys. Rep., 663, 1
Strecker, A. 1850, Justus Liebigs Ann. Chem., 75, 27
Szopa, C., Cernogora, G., Boufendi, L., Correia, J. J., & Coll, P. 2006, Planet. Space Sci., 54, 394
Trainer, M. G., Pavlov, A. A., Curtis, D. B., et al. 2004, Astrobiology, 4, 409
Trainer, M. G., Pavlov, A. A., Dewitt, H. L., et al. 2006, PNAS, 103, 18035
Tsai, S.-M., Malik, M., Kitzmann, D., et al. 2021, ApJ, 923, 264
Van Eylen, V., Agentoft, C., Lundkvist, M. S., et al. 2018, MNRAS, 479, 4786
Venot, O., Fray, N., Bénilan, Y., et al. 2013, A&A, 551, A131
Venot, O., Bénilan, Y., Fray, N., et al. 2018, A&A, 609, A34
Venot, O., Cavalié, T., Bounaceur, R., et al. 2020, A&A, 634, A78
Wang, S., Yang, Z., He, C., et al. 2025, ApJ, 990, 187
Wen, J.-S., Pinto, J. P., & Yung, Y. L. 1989, J. Geophys. Res., 94, 14957
Wogan, N. F., Batalha, N. E., Zahnle, K. J., et al. 2024, ApJ, 963, L7
Yang, J., & Hu, R. 2024, ApJ, 971, L48
Yang, Z., Liu, Y., He, C., et al. 2025, Planet. Sci. J., 6, 47
Zhan, Z., Huang, J., Seager, S., Petkowski, J. J., & Ranjan, S. 2022, ApJ, 930, 133

Appendix A: Experimental identification of species

We report here the MS fragmentation patterns of hydrocarbon compounds with two and three atoms (Figure A.1), the reference IR spectra from the HITRAN database (Figure A.2) and the main MS and IR features used to identity products (Table A.1).

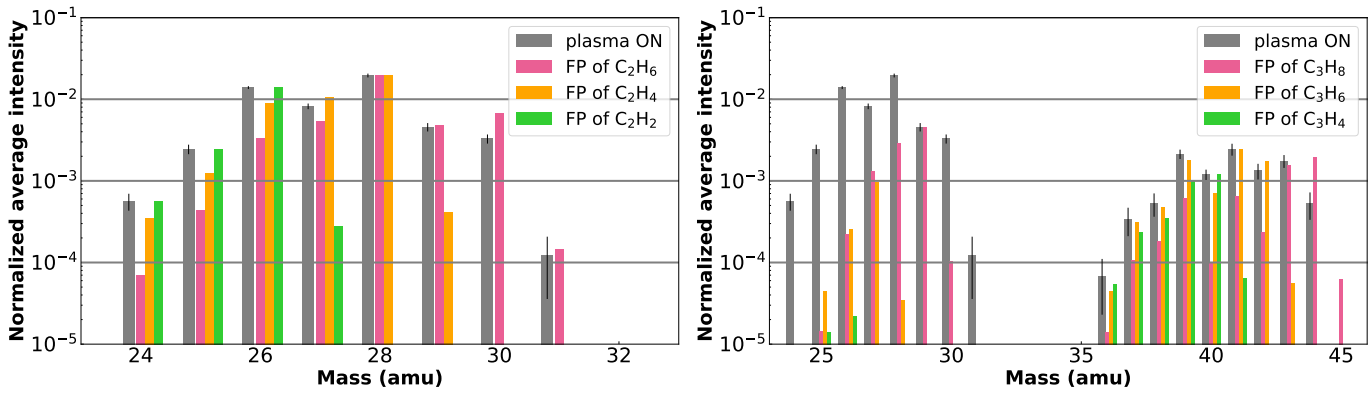

(a) (b)

Fig. A.1: Mass spectrum of an irradiated gas mixture of 95% H_2 + 5% CH_4 (Gray). Fragmentation patterns (FP) of the two-carbon atoms (A.1a) and three-carbon atoms (A.1b) compounds (Pink for the alkanes, orange for the alkenes, green for the alkynes). Each FP is normalized to the intensity of the experimental spectrum at the m/z value corresponding to the most intense peak of the FP. 95% uncertainty bars are displayed in black.

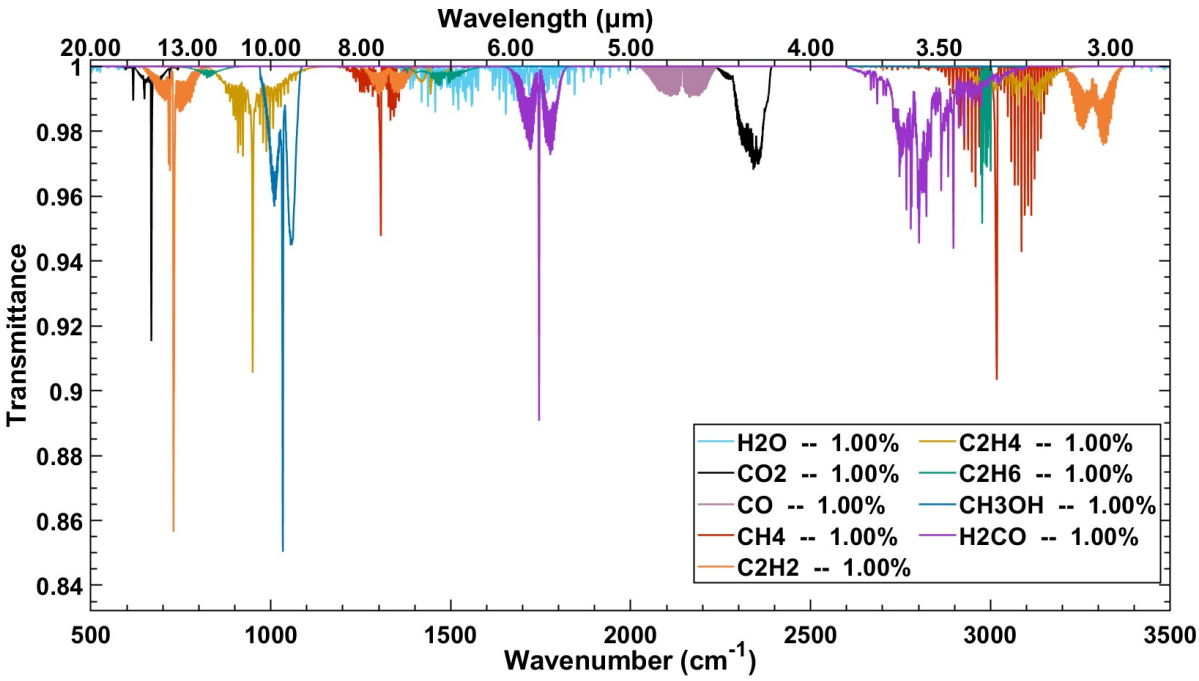

Fig. A.2: Infrared features calculated from the HITRAN database for molecules with up to 2 carbon atoms studied in this study, with a fixed composition of 1% for each of them in a gas mixture of 1 mbar at 340 K.

Table A.1: Features of products identified by MS and IR spectroscopy.

Molecules	**Main MS features (u)**	**Main IR features (cm^{-1})**	**Main IR features (μm)**
C_2H_2	26 - 25 - 24 - 27 - 28	730 [p]	13.70 [p]
C_2H_4	28 - 27 - 26 - 25 - 24	950 [p]	10.53 [p]
C_2H_6	28 - 27 - 30 - 29 - 26	2900->3000 [s] - 1300->1600 [s]	3.45->3.33 [s] - 7.69->6.25 [s]
$CH_2C_2H_2$	40 - 39 - 38 - 37 - 36	1910->1990 [s]	5.24->5.03 [s]
CH_3C_2H	40 - 39 - 38 - 37 - 36	633 [p] - 2100->2200 [s]	15.80 [p] - 4.76->4.55 [s]
C_3H_6	41 - 39 - 42 - 27 - 40	912 [p]	10.96 [p]
C_3H_8	29 - 28 - 27 - 44 - 43	2900->3000 [s] - 1300->1600 [s]	3.45->3.33 [s] - 7.69->6.25 [s]
H_2CO	29 - 30 - 28	1745 [p]	5.73 [p]
CH_3OH	31 - 32 - 29 - 15	1033 [p]	9.68 [p]
CH_3CHO	29 - 44 - 43 - 15	1745 [s]	5.73 [s]

[p] : single peak, narrow [s] : set of peaks, broad